



A density functional theory study of reactions of relevance to catalytic hydrocarbon synthesis and combustion

Mina Arya^{1,2} · Joakim Niklasson¹ · Abas Mohsenzadeh¹ · Kim Bolton¹

Received: 25 June 2018 / Accepted: 25 September 2018 / Published online: 17 October 2018
© The Author(s) 2018

Abstract

Synthesis and combustion of hydrocarbons on a series of metal surfaces (Ag, Au, Al, Cu, Rh, Pt and Pd) were investigated using density functional theory (DFT). The adsorption energies for all species involved in these reactions, as well as the reaction energies and activation barriers on these surfaces, were calculated using the same models and DFT methods. The results were used to test the validity of the Brønsted–Evans–Polanyi (BEP) and transition state scaling (TSS) relationships for these reactions on these metal surfaces. The BEP relationship appears to be a valid indicator for the synthesis reactions with R^2 values of 0.83, 0.88 and 0.94 for CO dissociation, CO hydrogenation and formyl (CHO) dissociation to CH + O, respectively. In addition to CH splitting, which has been studied before, the BEP relationship also appears to be valid for the CH oxidation and CHO dissociation to CO + H combustion reactions with R^2 values of 0.94, 0.89 and 0.88, respectively. Also, the TSS relationship is excellent with a R^2 value of 1 for all synthesis and combustion reactions. The BEP and TSS relationships were subsequently used to estimate the energetics of the synthesis and combustion reactions on Ni, Co and Fe surfaces. The results reveal that the transition state energies estimated by the TSS relationships are in better agreement with data obtained from DFT calculations than the activation energies estimated by the BEP relationships. Therefore, the TSS relationship is preferred when predicting energetics of these reactions on these surfaces.

Keywords Density functional theory · Hydrocarbon synthesis · Hydrocarbon combustion · Brønsted–Evans–Polanyi · Transition state scaling · Catalyst

Electronic supplementary material The online version of this article (<https://doi.org/10.1007/s00214-018-2339-4>) contains supplementary material, which is available to authorized users.

✉ Mina Arya
mina.arya@hb.se

Joakim Niklasson
s161931@student.hb.se

Abas Mohsenzadeh
abas.mohsenzadeh@hb.se

Kim Bolton
kim.bolton@hb.se

¹ Swedish Centre for Resource Recovery, University of Borås, 501-90 Borås, Sweden

² Department of Chemistry, University of Sistan and Baluchestan, Zahedan 98135-674, Iran

1 Introduction

The interactions between atomic or molecular species and metal surfaces are fundamental to surface chemistry [1], and the field of modern theoretical surface science provides an opportunity to investigate adsorbates and surface structures on the microscopic scale. The insight gained at this scale has useful applications in industrial technologies, including the search for more efficient catalysts [2]. There are numerous reviews and articles which deal with adsorption of small molecules and radicals on metal surfaces, from both experimental and theoretical studies [3–11].

A complete mechanistic study of surface reactions requires the identification of the elementary processes, including the reaction intermediates. Hydrocarbon synthesis from carbon monoxide and hydrogen (synthesis gas which is often referred to as syngas) is probably the most important source for manufacturing fuels and chemicals from non-petroleum-based sources [12]. Fischer–Tropsch synthesis (FTS) converts the syngas into high molecular weight

hydrocarbons, which can subsequently be transformed into high-quality chemicals and ultraclean fuels [13, 14]. Various mechanisms have been proposed for the hydrocarbon chain initiation and growth steps [15]. One is the carbide mechanism, where CO dissociation precedes hydrogenation of the chemisorbed carbon atom to form CH_x monomers that initiate the growth of hydrocarbon chains [16]. Hence, the dissociation of the surface-adsorbed CO molecule is an important step in the Fischer–Tropsch reaction [15].

Formyl (CHO) is also an important intermediate in hydrocarbon synthesis, FTS and hydrocarbon combustion [17, 18]. In contrast to hydrocarbon synthesis, the catalytic combustion of hydrocarbons is a very important technology for efficient energy production [19]. The main reaction pathway of catalytic combustion of hydrocarbons is the reaction between methylidyne (CH) and oxygen (O) to form formyl (CHO) [20]. This CHO species subsequently decomposes to yield adsorbed carbon monoxide and hydrogen ($\text{CHO} \rightarrow \text{CO} + \text{H}$) [18].

Gomes et al. [20] studied adsorption of the formyl species on Cu, Au and Pt (111) surfaces using density functional theory (DFT) and where the metals are modelled as clusters. They found that the adsorption energy of formyl on the Au surface is very small (-0.54 eV) and characteristic of a physisorbed species, whereas the interaction between CHO and the Pt surface is very strong (with an adsorption energy of -2.61 eV). The calculated CHO adsorption energy on the Cu surface is approximately -1.45 eV.

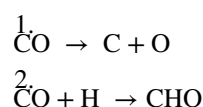
Inderwildi et al. [21] used DFT with the PW91 functional to study the mechanisms of hydrocarbon synthesis and combustion on noble metals. They suggested that CHO is an essential intermediate species in both synthesis and combustion reactions, and that these reactions have very similar mechanisms but in opposite directions, irrespective of the metal used to catalyze the reactions. Zhao et al. [22] also used DFT with the PW91 functional to explore the role of CHO in syngas conversion to hydrocarbons and its dependence on the Co and Rh catalyst surfaces. They found that the activation energy for insertion of CHO into CH_x ($x = 1-3$) is the same, or even lower, than CO insertion or the formation of a C–C bond by combining two C atoms. The mechanism of dry reforming of methane on a Ni catalyst was studied by Zhu et al. [23] using DFT with the PW91 functional. This reaction includes the formation and decomposition of CHO. They showed that oxidation determines the overall reaction rates for both C and CH oxidation pathways.

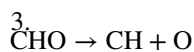
Mahmood et al. [24] used DFT with the PW91 functional to study CO adsorption on several low and high Miller index surfaces of Cu. They showed that the adsorption energy increases as the coordination number of the adsorption site decreases from 9 to 6, in qualitative agreement with experimental observations. They also found a large decrease in the adsorption energy with increased

surface coverage. The synthesis of formaldehyde and methanol from CO and H_2 on a Ni(111) catalyst was investigated by Remediakis et al. [25] using DFT based on the RPBE functional. They showed that when CO and H are adsorbed on Ni(111) surfaces, CO hydrogenation is favoured over CO dissociation or desorption since it has the lowest activation energy. Further hydrogenation leads to the formation of formaldehyde (CH_2O), methoxy (CH_3O) and, finally, methanol (CH_3OH).

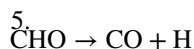
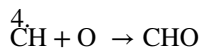
Despite the developments in theoretical modelling combined with improved computer hardware, it is still computationally expensive to calculate reaction and activation energies of industrially relevant processes. It is therefore of interest to be able to predict relevant energies using, for example, descriptor-based approaches. The existence of linear relations between the adsorption, reaction and activation energies is the basis of many of these approaches [26]. For example, it was recently established that the activation energy varies linearly with the reaction energy for dissociative chemisorption of a number of molecules on a wide range of metal surfaces [27–29]. The Brønsted–Evans–Polanyi (BEP) relationship is an empirical observation that, for an elementary reaction, there is a linear relationship between the kinetics (activation barriers) and the thermodynamics (reaction energies). Similarly, the transition state scaling (TSS) relationship proposes a linear relation between the transition state energy and the initial (reactant) or final (product) state energy [30]. Fajin et al. [31] studied the generalized BEP relationships and descriptors for O–H bond cleavage of organic molecules on transition metal surfaces. They found that there is a linear relationship between the O–H bond breaking activation energy of RO–H compounds (R = organic moiety) on catalytic transition metal systems and the adsorption energy of the products. Consequently, the product's adsorption energy is a good descriptor for the activation barrier for the breaking RO–H bond on transition metal surfaces. Pederson et al. [32] used DFT with the RPBE functional to study scaling properties of adsorption energies for hydrogen-containing molecules on transition metal surfaces. Their database provided a linear scaling relation connecting the adsorption energy of molecules such as CH_x , NH_x , SH_x and OH_x to the C, N, S and O adsorption energies, respectively, on transition metal surfaces. BEP relationships have also been validated for C–O and C–C bond dissociation during methanol decomposition and for ethylene dehydrogenation and hydrogenation on different Pd overlayer surfaces [33].

In this contribution, systematic and comparative DFT calculations have been performed to obtain the adsorption, reaction and activation energies of hydrocarbon synthesis





on Ag, Au, Al, Cu, Rh, Pt and Pd face-centred-cubic (111) surfaces. These surfaces were chosen because they have been used in numerous experimental and computational efforts [34–38]. The same methods were used to study hydrocarbon combustion on these surfaces. The splitting of CH ($\text{CH} \rightarrow \text{C} + \text{H}$) has been studied by us previously [39], and those data are complemented in the present contribution by studying the following two combustion reactions.



The calculated energies are used to test the validity of the BEP and TSS relationships for these reactions on these metal surfaces. Since these relationships are seen to be valid for most of the reactions studied here, they are used to predict the energetics of these reactions on three new metal surfaces (Ni face-centred-cubic (111), Co hexagonal-closed-packed (111) and Fe body-centred-cubic (111) surfaces). The predicted values were compared to the same energies calculated from DFT, using the same models and methods that were used for the original surfaces. To the best of our knowledge this is the first time that the same models and methods are used for all of the above reactions and surfaces to investigate the mechanism of catalytic synthesis and combustion of hydrocarbons and to test the validity of the BEP and TSS relationships.

2 Computational methods and models

The Vienna ab initio simulation package (VASP) [40–45], using spin-polarized density functional theory, was used to obtain the results presented here. The exchange–correlation was treated within the generalized-gradient approximation (GGA) using the revised Perdew–Burke–Ernzerhof (RPBE) functional [27, 30, 32, 46, 47]. The interactions between valence electrons and ion cores were described using the projector-augmented wave method (PAW) [48–50]. The Kohn–Sham orbitals were expanded in a plane-wave basis set using a kinetic energy cut-off of 400 eV [13], and a $4 \times 4 \times 1$ Monkhorst–Pack grid of k -points [51] was used for the numerical integration in reciprocal space. A 0.1 eV Fermi smearing was used for the density of states calculations, and the convergence criteria for the geometry optimizations, which used a conjugate-gradient algorithm (CG), were 10^{-3} eV \AA^{-1} for the forces acting on the ions and 10^{-5} eV for the total energy [23]. Also, a dense $41 \times 41 \times 1$ k -point grid was used for the density of state calculations.

The parameters used in this work have been used in previous, successful calculations of similar catalytic reactions

[17, 52, 53]. In addition, calculations made both here and in our previous work [39] confirm that the trends presented here are converged with respect to all important parameters, such as the size of the unit cell, the energy cut-off and the k -point mesh.

The metal (111) surfaces were constructed using a three-layer slab with a 2×2 unit cell and periodic boundary conditions in two directions (xy plane) to model a semi-infinite crystal surface. The ionic positions in the uppermost two layers and the adsorbates [54] were allowed to relax, while those in the bottom layer of the slab were fixed to maintain the crystal structure of the bulk. A 10- \AA vacuum region was placed between the slabs (in the z direction) to ensure that the adsorbates do not interact with the neighbouring slab. Similar models have been used in previous studies of comparable systems [53].

The transition states were identified using the climbing image-nudged elastic band (CI-NEB) method [55, 56]. In this method, the lowest energy configurations of reactants and products were used as the initial and final states, and six images were created between these geometries using a linear interpolation [57]. A -5.0-eV \AA^{-2} spring force constant between images was used to relax all of the images until the maximum force acting on each ion was less than 0.1 eV \AA^{-1} .

The vibrational frequencies of the reactants, transition states and products were calculated using ionic displacements of 0.01 \AA and by diagonalizing the resulting Hessian matrix. Only the ionic positions of the adsorbates were displaced for these calculations. These frequencies were used to calculate the zero point vibrational energies (ZPVEs) and vibrational partition functions, as well as to confirm that the stationary structures were minimum energy structures (zero imaginary frequencies) or transition states (one imaginary frequency). The normal mode with the imaginary frequency was also analysed to ensure that this vibrational mode connected the reactants with the products.

The adsorption energies (E_{ads}) of the reactants and products were calculated as $E_{\text{ads}} = E_{(\text{slab}+\text{adsorbate})} - (E_{\text{adsorbate}} + E_{\text{slab}})$ where $E_{(\text{slab}+\text{adsorbate})}$ is the total energy of the slab-adsorbate(s) system, $E_{\text{adsorbate}}$ is the total energy of the isolated geometry optimized adsorbate(s) in vacuum, and E_{slab} is the total energy of the slab [58, 59]. All energies were ZPVE-corrected.

The rate constants (k) were estimated from transition state theory [60] using

$$k = \left(\frac{k_{\text{B}} T}{h} \right) \left(\frac{q^{\#}}{q} \right) e^{-\frac{E_{\text{a}}}{k_{\text{B}} T}} \quad (1)$$

where k_{B} is Boltzmann's constant, T is the absolute temperature, h is Planck's constant, and E_{a} is the ZPVE-corrected

activation energy. q and q^\ddagger are the partition functions for the reactants and transition state, respectively. The partition functions were calculated assuming harmonic vibrations.

There are four high symmetry adsorption sites on all surfaces studied here (shown in Panel a of Fig. 1) except Fe (111) (shown in Panel b of Fig. 1). The hcp hollow site (where the central metal atom is in the second surface layer) is labelled A, the top site is above the uppermost metal surface atom and is labelled B, the bridge site between two neighbouring atoms is labelled C, and the fcc hollow site (where the central atom is in the third surface layer) is labelled D. There are five high symmetry adsorption sites on the Fe (111) surface. These are the top site labelled B, a short bridge site labelled E, a long bridge site labelled F, a pseudo-threefold hollow site labelled G and rectangular fourfold hollow site labelled H.

Geometry optimizations were performed by placing the adsorbate, with different initial orientations, on each of the adsorption sites shown in Fig. 1 and subsequently optimizing the system to yield the lowest ZPVE-corrected energy structure. The site that yielded the lowest energy was the preferred adsorption site. The preferred sites, energies and geometries of co-adsorbed adsorbates were obtained by placing the adsorbates in the same periodic cell and in their lowest energy sites identified from the geometry optimizations of the individual adsorbates [52]. The reaction energies (ΔE) are the difference between product (final state) and reactant (initial state) energies ($\Delta E = E_{\text{FS}} - E_{\text{IS}}$), and the activation energies (E_a) are the difference between transition state and initial state energies ($E_a = E_{\text{TS}} - E_{\text{IS}}$).

3 Results and discussion

3.1 Adsorption energies of reactants and products

The ZPVE-corrected adsorption energies, E_{ads} , for CH, C and H have been previously calculated by us using the same

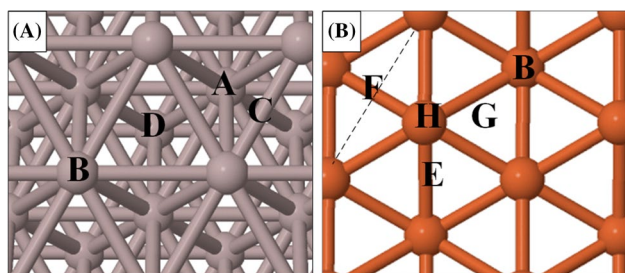


Fig. 1 Adsorption sites on the **a** Ag, Au, Al, Cu, Rh, Pt, Pd, Ni and Co (111) surfaces and **b** Fe (111) surface. A is an hcp site; B is a top site; C is a bridge site; D is a fcc site; E is a short bridge site; F is a long bridge site; G is a pseudo-threefold hollow site, and H is a rectangular fourfold hollow site

methods and models that are used in the present study [39]. E_{ads} , for the remaining species involved in the hydrocarbon synthesis and combustion reactions studied here, are presented in Table 1. Previously obtained computed and experimental data are shown for the sake of comparison. Details of the adsorption sites and geometries of the reactants, transition states and products are given in Tables S1–S3 in the supporting information.

The calculated CHO adsorption energies on these surfaces decrease in the order Ag > Cu > Au > Al > Pd > Rh > Pt. The highest adsorption energy (weakest adsorption) is on the Ag(111) surface and is -0.52 eV, compared to -2.14 eV on Pt (111). The preferred adsorption site for CHO is the top site for all surfaces except for Al, Rh and Pd where it is the fcc site for Al and bridge site for Rh and Pd. Similar trends in adsorption energies are reported in previous studies. For example, the CHO adsorption energies in the study by Lin et al. [35] decrease in the order Cu > Au > Ag > Pd > Rh > Pt, which, except for Ag, is in agreement with the trend seen in the present work. They found lower adsorption energies for CHO on all surfaces, and this difference is probably due to the fact that they used different super cell size, adsorption sites and exchange–correlation functional.

The calculated adsorption energies for CO vary from 0.16 eV on Au(111) to -1.50 eV on Pt(111) and decrease (become more negative) in the order Au > Ag > Al > Cu > Rh > Pd > Pt. The most stable adsorption site for CO is the fcc site for all surfaces except for Ag, Au and Al, where it is the top site for Ag and Al and the bridge site for Au. The trends in the calculated energies of CO adsorption are similar to those seen in previous studies. For example, the CO adsorption energies obtained by Hammer et al. [7] decreased in the order Ag > Au > Al > Cu > Pd > Pt, which is similar to the trend seen in the present work.

The calculated O adsorption energies decrease in the order Au > Ag > Pt > Pd > Cu > Rh > Al. The weakest adsorption is -2.40 eV on the Au (111) surface compared to -6.79 eV on the Al (111) surface. The preferred adsorption site for atomic oxygen is the fcc site for all surfaces. The O adsorption energies in a previous study by Liao et al. follow the same trend as that discussed in the present work (Au > Ag > Pd > Pt > Cu > Rh) except for Pd and Pt, which are very similar in the present study (-3.68 eV on Pt and -3.69 eV on Pd). The atomic oxygen adsorption energies reported by Liao et al. are more negative than those reported in this study, and the difference is probably due to the fact that they used different super cell size, adsorption sites and exchange–correlation functional.

The calculated (C + O) co-adsorption energies decrease in the order Ag > Au > Cu > Pt > Pd > Rh > Al. The weakest adsorption is -4.99 eV on the Ag (111) surface compared to -11.99 eV on the Al (111). Co-adsorption

Table 1 ZPVE-corrected adsorption and co-adsorption energies (eV) of all species involved in the hydrocarbon synthesis and combustion reactions. The references for the previously published data are given in the footnote to the table

Surface	CHO	CO	O	C+O	CO+H	CH+O
Ag						
Current work	-0.52	-0.01	-2.83	-4.99	-1.55	-5.28
Previous studies	-1.08 ^b	0.09 ^j	-3.60 ^a	-	-	-
Au						
Current work	-0.94	0.16	-2.40	-5.91	-1.62	-6.06
Previous studies	-1.51 ^b , -0.54 ⁱ	-0.04 ^j	-3.12 ^a	-	-	-
Al						
Current work	-1.70	-0.14	-6.79	-11.99	-1.86	-12.32
Previous studies	-	-0.49 ^j	-	-	-	-
Cu						
Current work	-0.84	-0.36	-4.07	-7.26	-2.46	-7.54
Previous studies	-1.43 ^b , -1.45 ⁱ	-1.30 ^c , -0.49 ^d , -0.62 ^g , -0.62 ^j	-5.07 ^a , -4.34 ^k	-	-	-
Rh						
Current work	-1.89	-1.36	-4.41	-10.43	-3.74	-10.14
Previous studies	-2.44 ^b	-1.67 ^g	-6.67 ^a	-	-	-
Pt						
Current work	-2.14	-1.50	-3.68	-9.01	-3.86	-8.99
Previous studies	-2.61 ^b , -2.61 ⁱ	-1.56 ^g , -1.45 ^j	-4.24 ^a	-	-	-
Pd						
Current work	-1.78	-1.48	-3.69	-9.20	-3.84	-8.67
Previous studies	-2.32 ^b	-1.96 ^e , -1.56 ^f , -1.60 ^g , -1.65 ^h , -1.30 ^j	-3.98 ^e , -3.49 ^f , -4.09 ^a	-	-	-

^aRef. [34] (the non-local corrections were based on Becke's gradient functional for exchange and Perdew's gradient functional for correlation, using a two-layer slab)

^bRef. [35] (GGA-PW91 calculations using a 4×4 unit cell and five-layer slab)

^cRef. [36] (GGA-PW91 calculations using a 3×3 unit cell and five-layer slab)

^dRef. [37] (experimental data from thermal desorption spectroscopy)

^eRef. [61] (GGA-PBE calculations using a 2×2 unit cell and three-layer slab)

^fRef. [61] (GGA-RPBE calculations using a 2×2 unit cell and three-layer slab)

^gRef. [62] (GGA-PBE calculations using a 2×4 unit cell and five-layer slab)

^hRef. [47] (GGA-RPBE calculations using a 2×2 unit cell and three-layer slab)

ⁱRef. [20] (DFT-B3LYP calculations using a 2×2 unit cell and three-layer slab)

^jRef. [7] (GGA-RPBE calculations using a 2×2 unit cell and three-layer slab)

^kRef. [63] (GGA-RPBE calculations using a 2×2 unit cell and three-layer slab)

data for these species, as well as those discussed below, have not been reported previously, and hence comparison with other studies is not possible.

For (CO + H) co-adsorption on these surfaces, E_{ads} range from -1.55 eV on Ag (111) to -3.86 eV on Pt (111) and decrease in the order Ag > Au > Al > Cu > Rh > Pd > Pt. The co-adsorption energy is therefore highest

on the Ag (111) surface, which was also seen for the CH, C and H adsorbates.

The calculated (CH + O) co-adsorption energies range from -5.28 eV on the Ag (111) surface to -12.32 eV on the Al (111) and decrease in the order Ag > Au > Cu > Pd > Pt > Rh > Al.

The weakest adsorption is on the Ag (111) surface for all species, except for the CO and O species, where it is on the Au (111) surface. In contrast, the strongest adsorption is on the Pt (111) surface for all species except for the CH, O, C+O and CH+O species, where it is on the Rh (111) for the CH species and on the Al (111) for the O, C+O and CH+O species. Co-adsorption data for the products of CO and CHO splitting have not been reported previously, and hence, comparison with other studies is not possible.

4 Reaction and activation energies

4.1 Catalytic hydrocarbon synthesis

The reaction energies, activation barriers and rate constants at 600 K, which is typical for industrial low-temperature catalytic reactions of hydrocarbons [64–66], for hydrocarbon synthesis are shown in Table 2.

The results in Table 2 show that the reaction energies for dissociation of CO decrease in the order Ag > Au > Cu > Pt > Pd > Rh > Al. The reaction is endothermic on all surfaces except for the Al (111) surface, where it is exothermic with a reaction energy -0.87 eV.

The calculated activation energies for dissociation of CO decrease in the order Ag > Au > Pd > Cu > Rh > Pt > Al, which is similar to the order for the reaction energies. The highest activation energy for CO splitting, obtained on the Ag (111) surface, was 6.05 eV, compared to 2.01 eV on Al (111).

The reaction rate constants for the CO dissociation are strongly influenced by the different metal surfaces, and at 600 K, they decrease from $1.93 \times 10^6 \text{ s}^{-1}$ on Al (111) to $1.99 \times 10^{-39} \text{ s}^{-1}$ on Ag (111). Thus, Al is the most active catalyst for CO splitting at 600 K. The trend in rate constants follows the opposite trend to the activation energies, with a higher activation energy leading to a lower rate constant.

The reaction energies for CO hydrogenation decrease in the order Pd > Rh > Pt > Cu > Ag > Au > Al. The

reaction on the Ag, Cu, Rh, Pt and Pd (111) surfaces is endothermic, while it is exothermic on the Au and Al(111) surfaces with reaction energies of -0.21 eV and -0.74 eV, respectively.

The activation energy for this reaction ranges from 1.32 eV on Rh (111) to 0.29 eV on Al (111) and decreases in the order Rh > Pd > Pt > Cu > Au > Ag > Al. The calculated reaction rate constants decrease in the opposite order to the activation energies. Thus, Rh and Pd are the least active catalysts and Al (111) is the most active catalyst for CO hydrogenation at 600 K.

The reaction energy of formyl dissociation to CH and O decreases in the order of Ag > Au > Cu > Pd > Pt > Rh > Al. This reaction follows the same order as CO dissociation, except for Pd and Pt. The reaction is endothermic on all surfaces except for the Al (111) surface, where it is exothermic with a reaction energy of -2.12 eV.

The calculated activation energies for dissociation of CHO to CH and O decrease in the order Au > Ag > Pt > Pd > Cu > Rh > Al. The highest activation energy obtained on the Au (111) surface was 3.88 eV, compared to 0.42 eV on Al (111). The reaction rate constant ranges from $9.46 \times 10^8 \text{ s}^{-1}$ on Al (111) to $4.07 \times 10^{-22} \text{ s}^{-1}$ on Au (111). Similarly to the two reactions discussed above, the trend in rate constants follows the opposite trend to the activation energies, with a higher activation energy leading to a lower rate constant. Al (111) is the most active catalyst for dissociation of CHO to CH and O.

For all three reactions studied here, the lowest reaction energy is on the Al (111) surface and the highest reaction energy is on Ag (111), except for the CO hydrogenation where it is on Pd (111). The trends of the reaction energies for the CO \rightarrow C+O and CHO \rightarrow CH+O reactions are the same except for Pd and Pt. The smallest activation energy, and consequently the highest reaction rate constant, is on Al (111) surface for all synthesis reactions. Al (111) is therefore the most active catalyst for all three reactions.

Figure 2 shows the geometries of the reactants, transition states and products of the species that are discussed with

Table 2 Reaction and activation energies (eV) and reaction rate constants at 600 K (s^{-1}) for the hydrocarbon synthesis reactions. The energies are ZPVE-corrected. Reaction and activation energies for these reactions have not previously been reported

Catalytic hydrocarbon synthesis									
Surface	CO \rightarrow C+O			CO+H \rightarrow CHO			CHO \rightarrow CH+O		
	ΔE	E_a	k	ΔE	E_a	k	ΔE	E_a	k
Ag	5.98	6.05	1.99×10^{-39}	0.13	0.53	1.09×10^9	3.73	3.77	9.61×10^{-21}
Au	5.03	5.05	4.43×10^{-31}	-0.21	0.64	1.12×10^8	3.37	3.88	4.07×10^{-22}
Al	-0.87	2.01	1.93×10^6	-0.74	0.29	1.1×10^9	-2.12	0.42	9.46×10^8
Cu	4.08	4.10	2.89×10^{-23}	0.72	0.85	7.90×10^5	1.80	2.03	7.95×10^{-8}
Rh	1.90	3.97	6.80×10^{-22}	0.95	1.32	1.85×10^2	0.24	1.61	7.32×10^{-2}
Pt	3.46	3.3	2.50×10^{-16}	0.83	1.11	3.40×10^3	1.50	2.49	7.96×10^{-10}
Pd	3.25	4.31	1.64×10^{-24}	1.16	1.31	3.92×10^2	1.61	2.4	1.62×10^{-8}

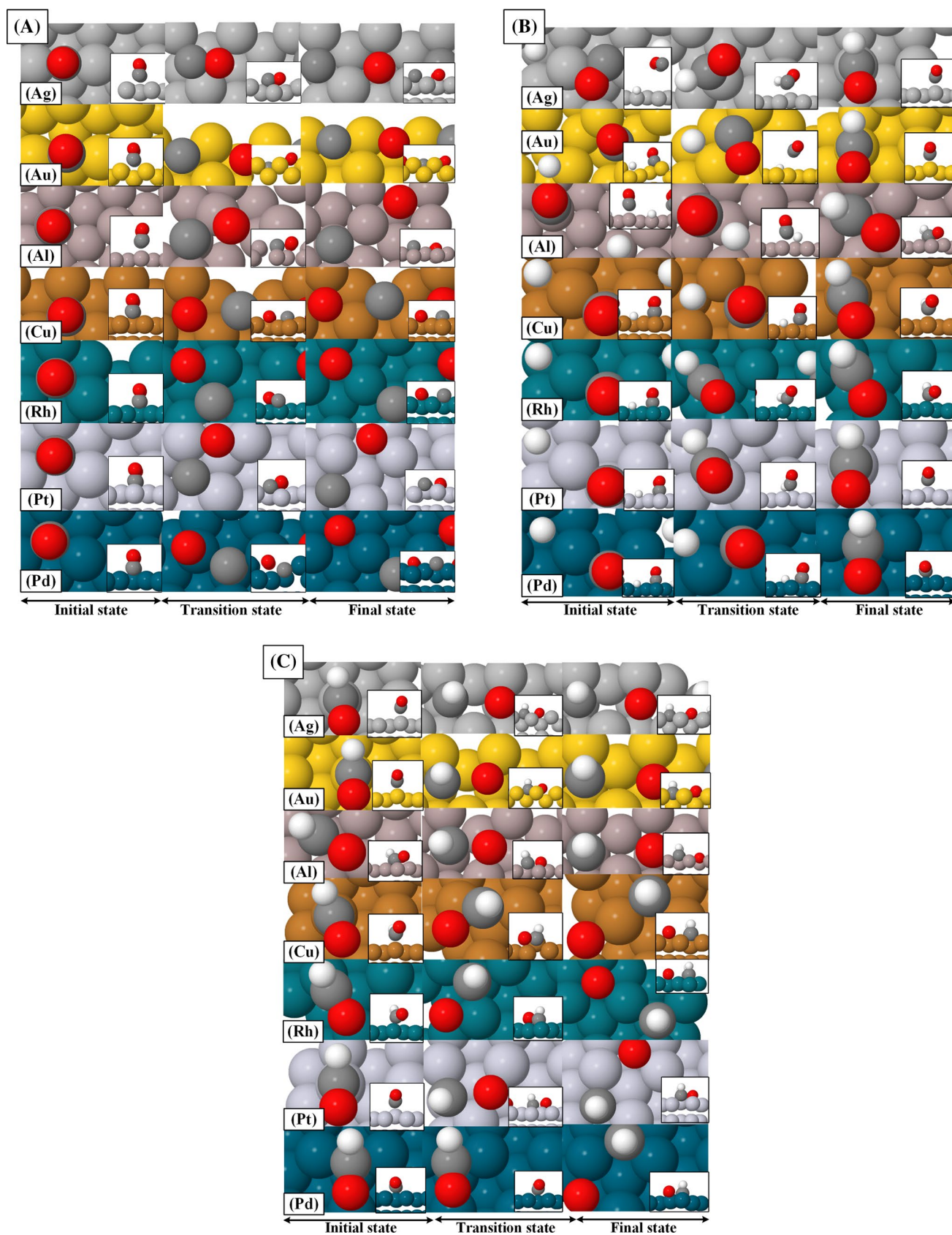


Fig. 2 Top and side views of the optimized structures for the initial, transition and final states for the **a** $\text{CO} \rightarrow \text{C} + \text{O}$, **b** $\text{CO} + \text{H} \rightarrow \text{CHO}$ and **c** $\text{CHO} \rightarrow \text{CH} + \text{O}$ reactions

reference to Table 2. Data for the $\text{CH} \rightarrow \text{C} + \text{H}$ reaction is not shown here since it has been presented elsewhere [39].

4.1.1 Catalytic hydrocarbon combustion

The reaction and activation energies for the hydrocarbon combustion reactions studied here, as well as the reaction rate constants at 600 K, are listed in Table 3 together with results of previous studies when available.

The reaction energies for CHO dissociation to CO and H decrease in the order $\text{Al} > \text{Au} > \text{Ag} > \text{Cu} > \text{Pt} > \text{Rh} > \text{Pd}$. The highest reaction energy, obtained on the Al (111) surface, was 0.64 eV, compared to -1.16 eV on Pd (111). The reaction on the Ag, Cu, Rh, Pt and Pd (111) is exothermic, while it is endothermic on the Au and Al (111) surfaces. Similar reaction energies are reported in the previous studies by Inderwildi et al. [21]. They found exothermic reaction energies on the Rh (111), Pt (111) and Pd (111) surfaces of -1.33 eV, -0.89 eV and -1.16 eV compared to -0.95 eV, -0.89 eV and -1.16 eV obtained here, respectively.

The activation energy for this reaction decreases in the order $\text{Al} > \text{Au} > \text{Ag} > \text{Rh} > \text{Pt} > \text{Pd} > \text{Cu}$. It ranges from 0.93 eV on the Al (111) surface to 0.13 eV on the Cu (111) surface. The calculated activation energies are comparable with most of the previous results. Inderwildi et al. [21] reported activation energies of 0.30, 0.57 and 0.36 eV for the Rh, Pt and Pd (111) surfaces, respectively, compared to 0.37, 0.28 and 0.14 eV in this work. As discussed above, these differences may be due to difference in the functionals and system sizes used in the studies.

The reaction rate constants at 600 K decrease from $3.02 \times 10^{12} \text{ s}^{-1}$ on Pd (111) to $1.03 \times 10^5 \text{ s}^{-1}$ on Al (111) and decrease in the order $\text{Pd} > \text{Ag} > \text{Rh} > \text{Pt} > \text{Cu} > \text{Au} > \text{Al}$. Pd (111) is the most active catalyst for CHO dissociation.

The results in Table 3 show that the reaction energies for oxidation of CH decrease in the order $\text{Al} > \text{Rh} > \text{Pt} > \text{Pd} > \text{Cu} > \text{Au} > \text{Ag}$. The lowest reaction energy for CH oxidation, obtained on the Ag (111) surface, was -3.73 eV, compared to 2.12 eV on Al (111). This reaction is exothermic on the all surfaces except for Al, where it is endothermic. Inderwildi et al. [21] obtained reaction energies of -0.14 eV, -1.18 eV and -1.38 eV on the Rh (111), Pt (111) and Pd (111) surfaces, respectively, which are similar to the values obtained in this work of -0.24 eV, -1.50 eV and -1.61 eV. As discussed above, these differences may be due to differences in the system sizes and functionals used in the studies.

The calculated activation energies for CH oxidation decrease in the order $\text{Al} > \text{Rh} > \text{Pt} > \text{Pd} > \text{Au} > \text{Cu} > \text{Ag}$. The highest activation energy for CH oxidation, obtained on the Al (111) surface, was 2.53 eV, compared to 0.04 eV on Ag (111) surface. The results presented here are in agreement with those obtained previously. For example, Inderwildi et al. [21] reported activation energies of 1.15, 1.12 and 0.78 eV for the Rh, Pt and Pd (111) surfaces, respectively. These can be compared to 1.37, 0.98 and 0.79 eV obtained in this work. Some activation energies reported by Inderwildi et al. are higher than those reported in this study, and the difference is probably due to the fact that they used different super cell size, adsorption sites and exchange–correlation functional.

Table 3 Reaction and activation energies (eV) and reaction rate constants at 600 K (s^{-1}) for the hydrocarbon combustion reactions. The energies are ZPVE-corrected

Surface		Catalytic hydrocarbon combustion						
		CHO \rightarrow CO + H			CH + O \rightarrow CHO			
		ΔE	E_a	k	ΔE	E_a	k	
Ag	Current work	-0.13	0.53	4.34×10^{10}	-3.73	0.04	3.83×10^{12}	
	Previous studies	–	–	–	–	–	–	
Au	Current work	0.21	0.84	6.15×10^5	-3.37	0.51	5.60×10^8	
	Previous studies	–	–	–	–	–	–	
Al	Current work	0.64	0.93	1.03×10^5	2.12	2.53	4.17×10^{-9}	
	Previous studies	–	–	–	–	–	–	
Cu	Current work	-0.72	0.13	8.28×10^9	-1.80	0.24	1.11×10^{11}	
	Previous studies	–	–	–	–	–	–	
Rh	Current work	-0.95	0.37	3.35×10^{10}	-0.24	1.37	3.89×10^1	
	Previous studies	-1.33^a	0.30^a	–	-0.14^a	1.15^a	–	
Pt	Current work	-0.83	0.28	9.01×10^9	-1.50	0.98	1.04×10^5	
	Previous studies	-0.89^a	0.57^a	–	-1.18^a	1.12^a	–	
Pd	Current work	-1.16	0.14	3.02×10^{12}	-1.61	0.79	2.62×10^6	
	Previous studies	-1.16^a	0.36^a	–	-1.38^a	0.78^a	–	

^aRef. [21] (GGA-PBE calculations using a 2×2 unit cell and three-layer slab)

The reaction rate constant at 600 K ranges from $3.83 \times 10^{12} \text{ s}^{-1}$ on Ag (111) to 4.17×10^{-9} on Al (111) and decreases in the order Ag > Cu > Au > Pd > Pt > Rh > Al. The trend in rate constants follows the opposite trend to the activation energies, with a higher activation energy leading to a lower rate constant. Ag (111) is the most active catalyst for CH oxidation.

The highest reaction energy is obtained on the Al (111) surface for both combustion reactions. As for the synthesis reactions discussed before, the trend in rate constants for the combustion reactions follows the opposite trend to the activation energies, with a higher activation energy leading to a lower rate constant, except for $\text{CHO} \rightarrow \text{CO} + \text{H}$ reaction.

4.2 Brønsted–Evans–Polanyi (BEP) and transition state scaling (TSS) relationships

According to the BEP relationship, the activation energy of a chemical reaction is linearly proportional to its reaction energy [67], and according to the TSS relationship the transition state energy is linearly proportional to the final state or initial state energy. Figure 3 shows these correlations for the hydrocarbon synthesis and combustion reactions on the metal surfaces listed in Tables 1, 2, 3. This figure reveals that the synthesis reactions support the BEP relationship with R^2 values of 0.83, 0.88 and 0.94 for CO dissociation, CO hydrogenation and formyl dissociation to $\text{CH} + \text{O}$, respectively. The BEP relationships are also valid for the combustion reactions. The activation energies for CH oxidation and formyl dissociation to $\text{CO} + \text{H}$ are linearly proportional to the reaction energies with R^2 values of 0.89 and 0.88, respectively. As shown previously [39], the activation energy for the CH splitting combustion reaction is linearly proportional to the reaction energy with and R^2 of 0.94.

The TSS relationship is excellent with an R^2 value of 1 for all synthesis and combustion reactions.

The validity of the BEP and TSS relationships was also tested by using the equations shown in Fig. 3 to predict the activation energies from the reaction energies (BEP) and the transition state energies from the initial state energies (TSS) for three new metal surfaces. These were the Ni (face-centred-cubic (111)), Co (hexagonal-closed-packed (111)) and Fe (body-centred-cubic (111)) surfaces. The predictions were for all synthesis and combustion reactions studied here. The predicted values were subsequently compared with the values calculated using the methods and models described in Sect. 2. The DFT data are shown in Tables S1–S3 in the supporting information, and the initial, transition and final state structures are illustrated in Fig. 4.

The activation and transition state energies predicted by the BEP and TSS relationships, as well as those determined from DFT calculations, are shown in Table 4. It can be seen that the activation energies predicted by the

BEP relationships for the Ni, Co and Fe (111) surfaces are similar to the DFT values. Also, as shown before [39], the activation energies predicted by the BEP relationship for the $\text{CH} \rightarrow \text{C} + \text{H}$ combustion reaction on the Ni, Co and Fe surfaces are 1.20, 1.08 and 0.83 eV, respectively, which can be compared to the explicit DFT energies of 1.23, 1.08 and 0.79 eV. Similarly, the transition state energies predicted by the TSS relationship for this reaction are -69.70 , -87.93 and -92.45 eV on the Ni, Co and Fe surfaces, respectively, which can be compared to the explicit DFT energies of -69.98 , -87.88 and -92.57 eV, respectively. The average difference between the BEP-predicted E_a for all six synthesis and combustion reactions and the DFT-calculated E_a is 17.65%, with the best agreement for $\text{CH} \rightarrow \text{C} + \text{H}$ reaction on the Co surface with an error of 0.15% and the worst for the $\text{CHO} \rightarrow \text{CO} + \text{H}$ reaction on Co with an error of 89.47%.

There is only a 0.39% average difference between TSS-predicted E_{TS} and the DFT-calculated E_{TS} . The best agreement is for the $\text{CO} + \text{H} \rightarrow \text{CHO}$ reaction on the Co surface with error of 0.02% and the worst for the $\text{CHO} \rightarrow \text{CH} + \text{O}$ reaction on Ni with an error of 1.13%.

The R^2 values obtained for the BEP and TSS relationships (Fig. 3) and the average differences between the DFT-calculated values and the BEP- or TSS-predicted values, show that the TSS relationship appears to be a better predictor than the BEP relationship. Moreover, the TSS relationship may be preferred since the structure of either the final or initial state, and not both, is sufficient for estimating the activation barrier.

It may be noted that the BEP and TSS relationships were derived from DFT data obtained for the reactions on the surfaces of diamagnetic metals (Ag, Au, Al, Cu, Rh, Pt and Pd) and that they are used to test the resulting predictions for reactions on the surfaces of paramagnetic metals. The different magnetisms of these metals were taken into account in the calculations (by using $\text{ISPIN} = 1$ for the diamagnetic metals and $\text{ISPIN} = 2$ for the paramagnetic metals). In spite of this difference between the sampling and test groups, the predictions are very good. One can therefore expect the predictions made for other diamagnetic metals would be at least as good as the results presented here.

4.3 Analysis of trends in the adsorption and activation energies

The d-band centre, which demonstrates the ability to eject an electron from the d-band of the metal to the adsorbate, is obtained from the distribution of the surface electronic energy levels [68, 69]. It is calculated from the projected density of states (PDOS) of the d-orbitals and can be used to measure the proximity of the d-electrons to the Fermi level. It is a common way to try to understand trends in adsorption and activation energies of different metal

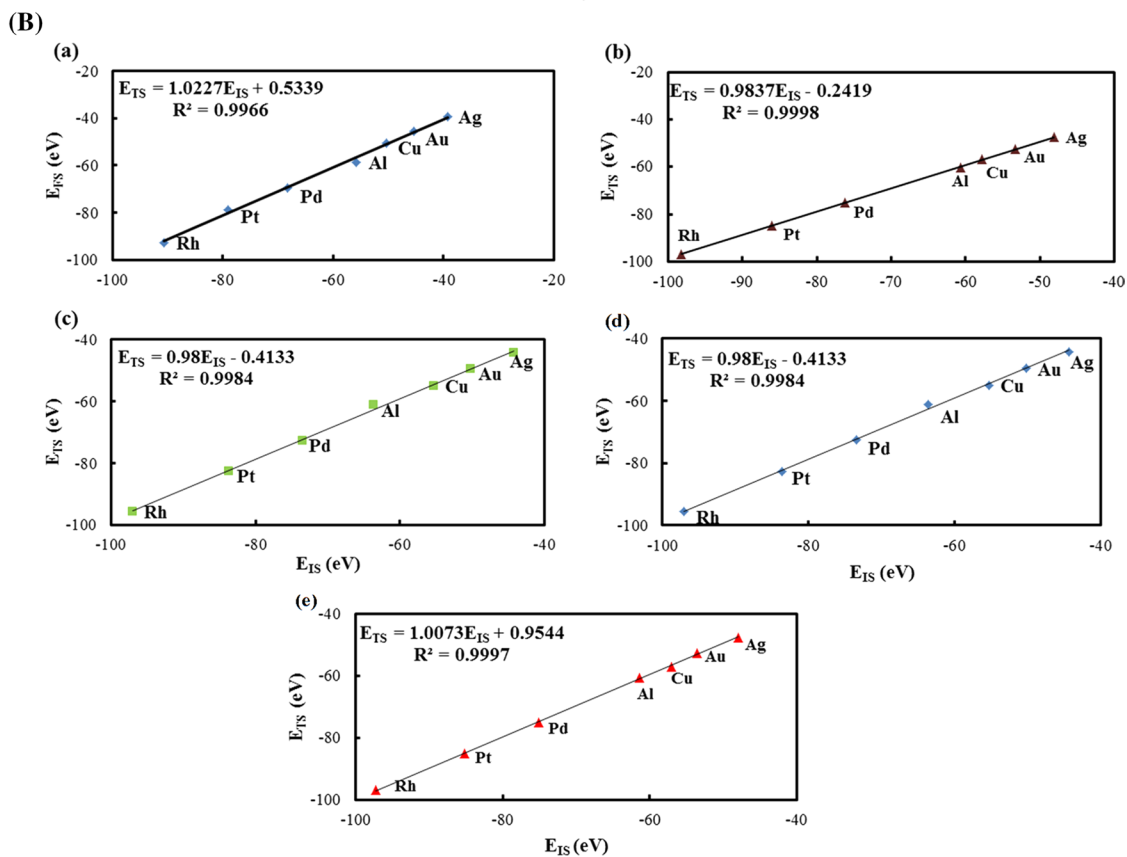
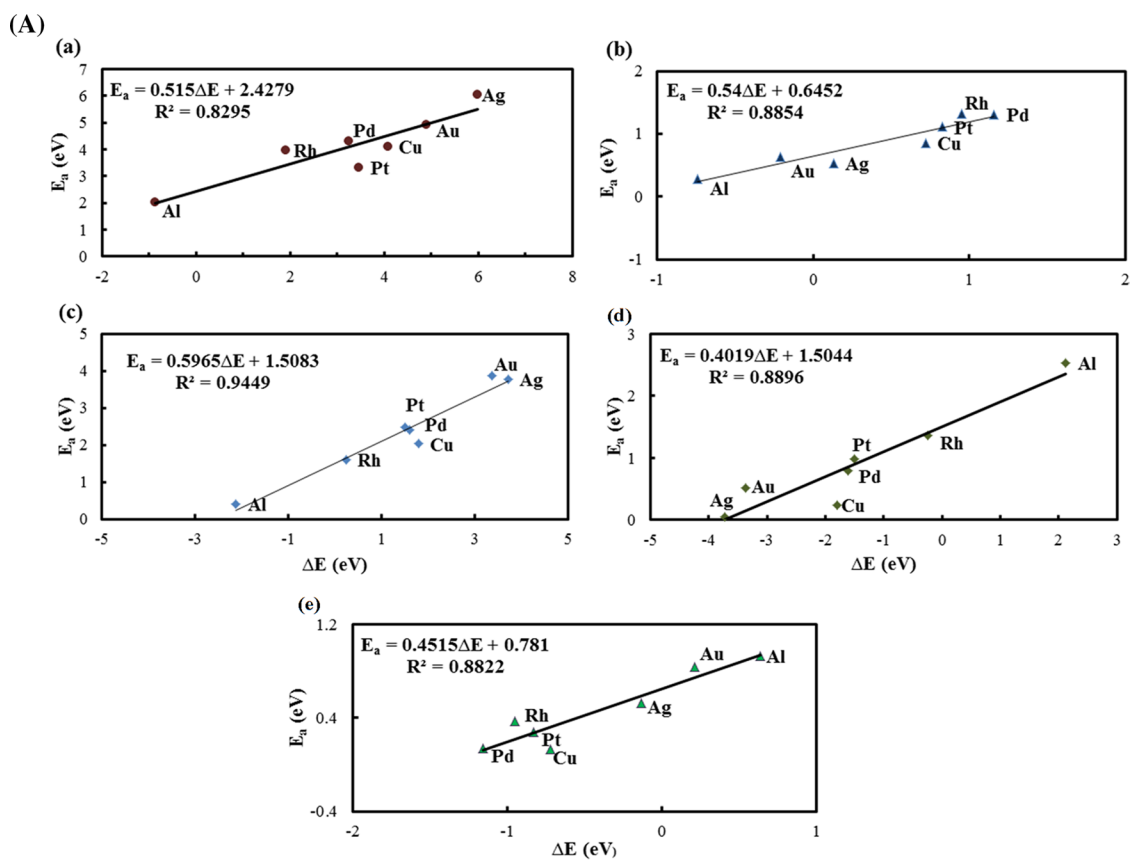


Fig. 3 (A) BEP and (B) TSS relationships for the **a** $\text{CO} \rightarrow \text{C} + \text{O}$, **b** $\text{CO} + \text{H} \rightarrow \text{CHO}$, **c** $\text{CHO} \rightarrow \text{CH} + \text{O}$, **d** $\text{CH} + \text{O} \rightarrow \text{CHO}$ and **e** $\text{CHO} \rightarrow \text{CO} + \text{H}$ reactions on the metallic surfaces listed in Table 1

surfaces. The projected density of states was calculated for the upper atomic layer of the metal surfaces studied here, and the results are given in Fig. S1 in supporting information. According to this figure, the adsorption energies would expect to decrease in the order $\text{Au} > \text{Ag} > \text{Cu} > \text{Pd} > \text{Pt} > \text{Rh}$. This is different to the ordering of the adsorption and activation energies of reactant, product and the transition states given above and hence does not explain the trends seen in this work. For example, the activation energies for the $\text{CH} + \text{O} \rightarrow \text{CHO}$ reaction decrease in the order $\text{Al} > \text{Rh} > \text{Pt} > \text{Pd} > \text{Au} > \text{Cu} > \text{Ag}$. Similar results are reported in previous studies. For example, Fajin et al. [68] reported that the d-band model cannot be used to understand the origin of the BEP relationship of water dissociation on different metal surfaces.

Another way to explain trends in adsorption and activation energies is the coordination number of the metal surface atoms. It is argued that adsorbates typically bind more strongly to surfaces with low coordination numbers [70–72]. Since the coordination numbers for all (111) surfaces studied here are identical, this is not able to explain the trends seen in the present work.

5 Conclusions

The thermodynamic and catalytic activity of Ag, Au, Al, Cu, Rh, Pt and Pd (111) metal surfaces for hydrocarbon synthesis and combustion has been examined using DFT calculations based on the RPBE functional. The results have been used to test the validity of the BEP and TSS relationships for these reactions on these metal surfaces. The BEP relationship appears to be an adequate indicator for the synthesis reactions with R^2 values of 0.83, 0.88 and 0.94 for CO dissociation, CO hydrogenation and CHO dissociation to $\text{CH} + \text{O}$. In addition to the $\text{CH} \rightarrow \text{C} + \text{H}$ combustion reaction, which has been studied previously [39], the BEP relationship also appears to be valid for the $\text{CH} + \text{O} \rightarrow \text{CHO}$ and $\text{CHO} \rightarrow \text{CO} + \text{H}$ combustion reactions with R^2 values of 0.89 and 0.88, respectively. It was also found that the TSS relationship is an excellent indicator with an R^2 value of 1 for all synthesis and combustion reactions.

The BEP and TSS relationships were subsequently used to estimate the energetics of the synthesis and combustion

reactions on Ni, Co and Fe (111) surfaces. As expected, the energies predicted by the TSS relationship are more accurate (closer to the DFT calculations) than those predicted by the BEP relationship. In fact, there is only a 0.39% average difference between TSS-predicted transition state and the DFT-calculated values, where this average is over all synthesis and combustion reactions and all three metal surfaces. This indicates that the TSS relationship can be used to predict transition state energetics for these reactions on these surfaces without doing the time-consuming transition state DFT calculations.

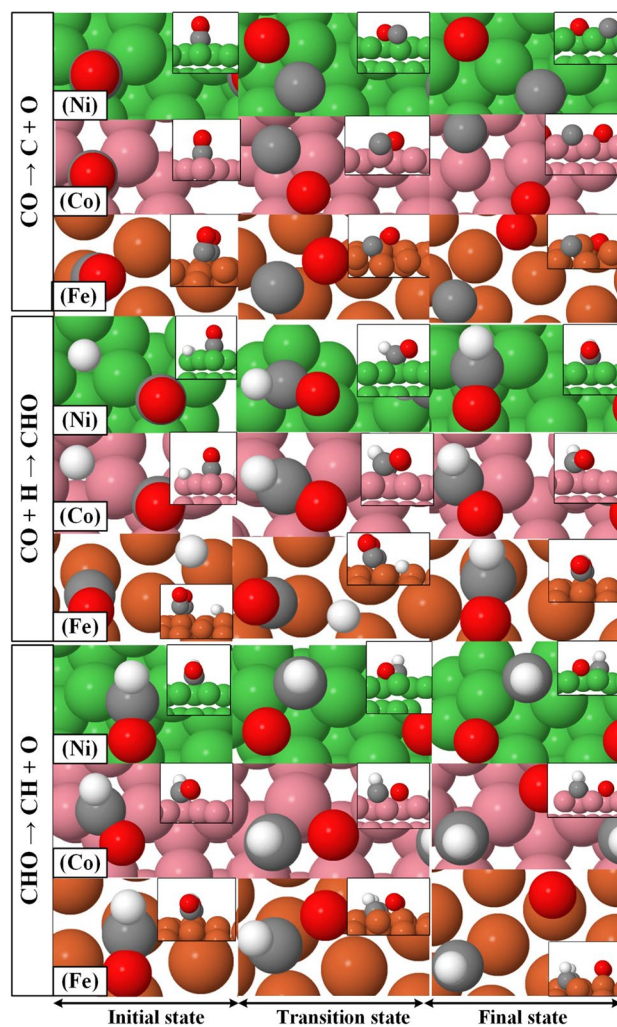


Fig. 4 Optimized structures for the initial, transition and final states for the synthesis reactions on the Ni, Co and Fe (111) surfaces

Table 4 BEP-predicted E_a , TSS-predicted E_{TS} and the corresponding energies explicitly calculated from DFT using the methods described in Sect. 2. All energies are in eV

	Reaction	Surface	BEP-predicted E_a	TSS-predicted E_{TS}	DFT-calculated E_a	DFT-calculated E_{TS}
Catalytic hydro-carbon synthesis	CO → C + O	Ni	3.49	-71.90	3.30	-72.43
		Co	3.11	-89.96	2.61	-90.73
		Fe	2.70	-94.34	2.26	-95.35
	CO + H → CHO	Ni	1.38	-78.45	1.52	-77.95
		Co	1.34	-95.74	1.31	-95.76
		Fe	0.96	-99.78	1.19	-99.99
		Ni	1.75	-76.01	1.24	-76.87
		Co	1.22	-94.15	0.76	-95.02
		Fe	1.75	-99.11	0.94	-99.67
Catalytic hydro-carbon combustion	CH + O → CHO	Ni	1.34	-76.57	0.84	-76.87
		Co	1.70	-94.75	1.24	-95.02
		Fe	1.34	-98.62	0.54	-99.67
	CHO → CO + H	Ni	0.16	-77.73	0.16	-77.95
		Co	0.19	-95.52	0.02	-95.76
		Fe	0.52	-100.38	0.61	-99.99

Acknowledgements The authors are very grateful for funding from Sparbanksstiftelsen Sjuhärads. The calculations were performed on resources provided by the Swedish National Infrastructure for Computing (SNIC) at the Uppsala Multidisciplinary Centre for Advanced Computational Science (UPPMAX).

Open Access This article is distributed under the terms of the Creative Commons Attribution 4.0 International License (<http://creativecommons.org/licenses/by/4.0/>), which permits unrestricted use, distribution, and reproduction in any medium, provided you give appropriate credit to the original author(s) and the source, provide a link to the Creative Commons license, and indicate if changes were made.

References

- Lewis SP, Rappe AM (1999) Structural and vibrational properties of carbon monoxide adlayers on the copper (001) surface. *J Chem Phys* 110(9):4619–4633
- Gajdoš M, Eichler A, Hafner J (2004) CO adsorption on close-packed transition and noble metal surfaces: trends from ab initio calculations. *J Phys: Condens Matter* 16(8):1141
- Meunier FC, Reid D, Goguet A, Shekhtman S, Hardacre C, Burch R, Deng W, Flytzani-Stephanopoulos M (2007) Quantitative analysis of the reactivity of formate species seen by DRIFTS over a Au/Ce (La) O₂ water–gas shift catalyst: first unambiguous evidence of the minority role of formates as reaction intermediates. *J Catal* 247(2):277–287
- Hirano H, Tanaka K-I (1992) A reason for the structure-insensitive catalytic activity of Ni (100) and Ni (111) surfaces for the methanation reaction of CO. *J Catal* 133(2):461–466
- Ledentu V, Dong W, Sautet P (2000) Heterogeneous catalysis through subsurface sites. *J Am Chem Soc* 122(8):1796–1801
- Hirano H, Tanaka K (1993) Structure and reactivity of carbidic intermediates for the methanation reaction on Ni (100), Ni (111) and Ni (110) surfaces. *Stud Surf Sci Catal* 75:1575–1578
- Hammer B, Morikawa Y, Nørskov JK (1996) CO chemisorption at metal surfaces and overlayers. *Phys Rev Lett* 76(12):2141
- Kresse G, Gil A, Sautet P (2003) Significance of single-electron energies for the description of CO on Pt (111). *Phys Rev B* 68(7):073401
- Thiel PA, Madey TE (1987) The interaction of water with solid surfaces: fundamental aspects. *Surf Sci Rep* 7(6–8):211–385
- Nöbl C, Benndorf C, Madey TE (1985) H₂O adsorption on Ni (100): evidence for oriented water dimers. *Surf Sci* 157(1):29–42
- Bunnik BS, Kramer GJ (2006) Energetics of methane dissociative adsorption on Rh 111 from DFT calculations. *J Catal* 242(2):309–318
- Fischer F, Tropsch H (1923) The preparation of synthetic oil mixtures (synthol) from carbon monoxide and hydrogen. *Brennst-Chem* 4:276–285
- Zhuo M, Tan KF, Borgna A, Saeys M (2009) Density functional theory study of the CO insertion mechanism for Fischer–Tropsch synthesis over Co catalysts. *J Phys Chem C* 113(19):8357–8365
- Cheng J, Hu P, Ellis P, French S, Kelly G, Lok CM (2008) Chain growth mechanism in Fischer–Tropsch synthesis: a DFT study of C–C coupling over Ru, Fe, Rh, and Re surfaces. *J Phys Chem C* 112(15):6082–6086
- Bromfield TC, Curulla Ferré D, Niemantsverdriet JW (2005) A DFT study of the adsorption and dissociation of CO on Fe (100): influence of surface coverage on the nature of accessible adsorption states. *ChemPhysChem* 6(2):254–260
- Ojeda M, Nabar R, Nilekar AU, Ishikawa A, Mavrikakis M, Iglesia E (2010) CO activation pathways and the mechanism of Fischer–Tropsch synthesis. *J Catal* 272(2):287–297
- Mohsenzadeh A, Bolton K, Richards T (2015) Oxidation and dissociation of formyl on Ni (111), Ni (110) and Ni (100) surfaces: a comparative density functional theory study. *Top Catal* 58(14–17):1136–1149
- Inderwildi OR, Jenkins SJ, King DA (2007) An unexpected pathway for the catalytic oxidation of methylidyne on Rh 111 as a route to syngas. *J Am Chem Soc* 129(6):1751–1759
- Yazawa Y, Takagi N, Yoshida H, S-i Komai, Satsuma A, Tanaka T, Yoshida S, Hattori T (2002) The support effect on propane combustion over platinum catalyst: control of the oxidation-resistance

- of platinum by the acid strength of support materials. *Appl Catal A* 233(1–2):103–112
20. Gomes JRB, Gomes J (2000) Adsorption of the formyl species on transition metal surfaces. *J Electroanal Chem* 483(1):180–187
 21. Inderwildi OR, Jenkins SJ, King DA (2008) Mechanistic studies of hydrocarbon combustion and synthesis on noble metals. *Angew Chem Int Ed* 47(28):5253–5255
 22. Zhao YH, Sun K, Ma X, Liu J, Sun D, Su HY, Li WX (2011) Carbon chain growth by formyl insertion on rhodium and cobalt catalysts in syngas conversion. *Angew Chem Int Ed* 50(23):5335–5338
 23. Zhu Y-A, Chen D, Zhou X-G, Yuan W-K (2009) DFT studies of dry reforming of methane on Ni catalyst. *Catal Today* 148(3):260–267
 24. Mehmood F, Kara A, Rahman TS, Bohnen KP (2006) Energetics of CO on stepped and kinked Cu surfaces: a comparative theoretical study. *Phys Rev B* 74(15):155439
 25. Remediakis IN, Abild-Pedersen F, Nørskov JK (2004) DFT study of formaldehyde and methanol synthesis from CO and H₂ on Ni (111). *J Phys Chem B* 108(38):14535–14540
 26. Grabow LC, Studt F, Abild-Pedersen F, Petzold V, Kleis J, Bligaard T, Nørskov JK (2011) Descriptor-based analysis applied to HCN synthesis from NH₃ and CH₄. *Angew Chem Int Ed* 50(20):4601–4605
 27. Nørskov JK, Bligaard T, Logadottir A, Bahn S, Hansen LB, Bollinger M, Benggaard H, Hammer B, Slijivancanin Z, Mavrikakis M (2002) Universality in heterogeneous catalysis. *J Catal* 209(2):275–278
 28. Pallassana V, Neurock M (2000) Electronic factors governing ethylene hydrogenation and dehydrogenation activity of pseudomorphic PdML/Re (0001), PdML/Ru (0001), Pd (111), and PdML/Au (111) surfaces. *J Catal* 191(2):301–317
 29. Liu Z-P, Hu P (2001) General trends in CO dissociation on transition metal surfaces. *J Chem Phys* 114(19):8244–8247
 30. Logadottir A, Rod TH, Nørskov JK, Hammer B, Dahl S, Jacobsen CJH (2001) The Brønsted–Evans–Polanyi relation and the volcano plot for ammonia synthesis over transition metal catalysts. *J Catal* 197(2):229–231
 31. Fajín JLC, Cordeiro MNDS, Illas F, Gomes JRB (2014) Generalized Brønsted–Evans–Polanyi relationships and descriptors for O–H bond cleavage of organic molecules on transition metal surfaces. *J Catal* 313:24–33
 32. Abild-Pedersen F, Greeley J, Studt F, Rossmeisl J, Munter TR, Moses PG, Skulason E, Bligaard T, Nørskov JK (2007) Scaling properties of adsorption energies for hydrogen-containing molecules on transition-metal surfaces. *Phys Rev Lett* 99(1):016105
 33. Santen RAV, Neurock M, Shetty SG (2009) Reactivity theory of transition-metal surfaces: a Brønsted–Evans–Polanyi linear activation energy–free-energy analysis. *Chem Rev* 110(4):2005–2048
 34. Liao M-S, Zhang Q-E (1998) Dissociation of methane on different transition metals. *J Mol Catal A: Chem* 136(2):185–194
 35. Lin C-H, Chen C-L, Wang J-H (2011) Mechanistic studies of water–gas-shift reaction on transition metals. *J Phys Chem C* 115(38):18582–18588
 36. Neef M, Doll K (2006) CO adsorption on the Cu (111) surface: a density functional study. *Surf Sci* 600(5):1085–1092
 37. Vollmer S, Witte G, Wöll C (2001) Determination of site specific adsorption energies of CO on copper. *Catal Lett* 77(1):97–101
 38. Huang S-C, Lin C-H, Wang JH (2010) Trends of water gas shift reaction on close-packed transition metal surfaces. *J Phys Chem C* 114(21):9826–9834
 39. Arya M, Mirzaei AA, Davarpanah AM, Barakati SM, Atashi H, Mohsenzadeh A, Bolton K (2018) DFT studies of hydrocarbon combustion on metal surfaces. *J Mol Model* 24(2):47. <https://doi.org/10.1007/s00894-018-3585-z>
 40. Kresse G, Hafner J (1993) Ab initio molecular dynamics for liquid metals. *Phys Rev B* 47(1):558
 41. Kresse G, Furthmüller J (1996) Efficiency of ab initio total energy calculations for metals and semiconductors using a plane-wave basis set. *Comput Mater Sci* 6(1):15–50
 42. Kresse G, Furthmüller J (1996) Efficient iterative schemes for ab initio total-energy calculations using a plane-wave basis set. *Phys Rev B* 54(16):11169
 43. Wan JF, Wang JN (2005) Structure dependence of optical spectra of ferromagnetic Heusler alloy Ni–Mn–Ga. *Physica B* 355(1):172–175
 44. Selvarani G, Selvaganesh SV, Krishnamurthy S, Kiruthika GVM, Sridhar P, Pitchumani S, Shukla AK (2009) A methanol-tolerant carbon-supported Pt–Au alloy cathode catalyst for direct methanol fuel cells and its evaluation by DFT. *J Phys Chem C* 113(17):7461–7468
 45. Termentzidis K, Hafner J (2007) CO adsorption on a Au/Ni (111) surface alloy—a DFT study. *J Phys: Condens Matter* 19(24):246219
 46. Andersson MP, Bligaard T, Kustov A, Larsen KE, Greeley J, Johannessen T, Christensen CH, Nørskov JK (2006) Toward computational screening in heterogeneous catalysis: pareto-optimal methanation catalysts. *J Catal* 239(2):501–506
 47. Hammer B, Hansen LB, Nørskov JK (1999) Improved adsorption energetics within density-functional theory using revised Perdew–Burke–Ernzerhof functionals. *Phys Rev B* 59(11):7413
 48. Blöchl PE (1994) Projector augmented-wave method. *Phys Rev B* 50(24):17953
 49. Pan Y, Zhang H, Shi D, Sun J, Du S, Liu F, Hj Gao (2009) Highly ordered, millimeter-scale, continuous, single-crystalline graphene monolayer formed on Ru (0001). *Adv Mater* 21(27):2777–2780
 50. Wang S-G, Cao D-B, Li Y-W, Wang J, Jiao H (2005) Chemisorption of CO₂ on nickel surfaces. *J Phys Chem B* 109(40):18956–18963
 51. Monkhorst HJ, Pack JD (1976) Special points for Brillouin-zone integrations. *Phys Rev B* 13(12):5188
 52. Mohsenzadeh A, Borjesson A, Wang J-H, Richards T, Bolton K (2013) The effect of carbon monoxide co-adsorption on Ni-catalysed water dissociation. *Int J Mol Sci* 14(12):23301–23314
 53. Mohsenzadeh A, Richards T, Bolton K (2015) A density functional theory study of hydrocarbon combustion and synthesis on Ni surfaces. *J Mol Model* 21(3):46
 54. Hu C, Ting S-W, Chan K-Y, Huang W (2012) Reaction pathways derived from DFT for understanding catalytic decomposition of formic acid into hydrogen on noble metals. *Int J Hydrogen Energy* 37(21):15956–15965
 55. Henkelman G, Jónsson H (2000) Improved tangent estimate in the nudged elastic band method for finding minimum energy paths and saddle points. *J Chem Phys* 113(22):9978–9985
 56. Henkelman G, Uberuaga BP, Jónsson H (2000) A climbing image nudged elastic band method for finding saddle points and minimum energy paths. *J Chem Phys* 113(22):9901–9904
 57. Ciobîcă IM, Kramer GJ, Ge Q, Neurock M, Van Santen RA (2002) Mechanisms for chain growth in Fischer–Tropsch synthesis over Ru (0001). *J Catal* 212(2):136–144
 58. Belosludov RV, Sakahara S, Yajima K, Takami S, Kubo M, Miyamoto A (2002) Combinatorial computational chemistry approach as a promising method for design of Fischer–Tropsch catalysts based on Fe and Co. *Appl Surf Sci* 189(3):245–252
 59. Mohsenzadeh A, Richards T, Bolton K (2015) A density functional theory study of hydrocarbon combustion and synthesis on Ni surfaces. *J Mol Model* 21(3):1–11

60. Fajín JLC, Cordeiro MNDS, Illas F, Gomes JRB (2009) Influence of step sites in the molecular mechanism of the water gas shift reaction catalyzed by copper. *J Catal* 268(1):131–141
61. Hammer B, Nørskov JK (2000) Theoretical surface science and catalysis—calculations and concepts. *Adv Catal* 45:71–129
62. Mason SE, Grinberg I, Rappe AM (2004) First-principles extrapolation method for accurate CO adsorption energies on metal surfaces. *Phys Rev B* 69(16):161401
63. Gokhale AA, Dumesic JA, Mavrikakis M (2008) On the mechanism of low-temperature water gas shift reaction on copper. *J Am Chem Soc* 130(4):1402–1414
64. Wu M, Wang X, Dai Q, Gu Y, Li D (2010) Low temperature catalytic combustion of chlorobenzene over Mn–Ce–O/ γ -Al₂O₃ mixed oxides catalyst. *Catal Today* 158(3):336–342
65. Li N, Gaillard F, Boréave A (2008) Electrochemical promotion of Ag catalyst for the low temperature combustion of toluene. *Catal Commun* 9(6):1439–1442
66. Enger BC, Holmen A (2012) Nickel and Fischer-Tropsch Synthesis. *Catalysis Reviews* 54(4):437–488
67. Evans MG, Polanyi M (1938) Inertia and driving force of chemical reactions. *Trans Faraday Soc* 34:11–24
68. Fajín JLC, Cordeiro MNDS, Illas F, Gomes JRB (2010) Descriptors controlling the catalytic activity of metallic surfaces toward water splitting. *J Catal* 276(1):92–100
69. Hammer B, Nørskov JK (1995) Electronic factors determining the reactivity of metal surfaces. *Surf Sci* 343(3):211–220
70. Lee WT, Ford L, Blowers P, Nigg HL, Masel RI (1998) Why do heats of adsorption of simple gases on platinum surfaces vary so little with surface structure? *Surf Sci* 416(1):141–151
71. Pang X-Y, Wang C, Zhou Y-H, Zhao J-M, Wang G-C (2010) DFT study of the structure sensitivity for the adsorption of methyl, methoxy, and formate on Ni (111), Ni (100), and Ni (110) surfaces. *J Mol Struct (Thoechem)* 948(1):1–10
72. Delbecq F, Sautet P (1993) Low-temperature adsorption of formaldehyde on a platinum (111) surface. A theoretical study. *Langmuir* 9(1):197–207